



Carbonation Resistance of Alkali-Activated Slag Under Natural and Accelerated Conditions

Marija Nedeljković¹ · Yibing Zuo¹ · Kamel Arbi² · Guang Ye¹

Published online: 16 February 2018

© The Author(s) 2018. This article is an open access publication

Abstract

In this paper, carbonation resistance of alkali-activated slag (AAS) pastes exposed to natural and accelerated conditions up to 1 year was investigated. Two aspects of carbonation mechanism were evaluated. The first was the potential carbonation of the main binding phases in finely powdered AAS pastes. The second was the reactivity and diffusivity of CO₂ within the bulk AAS paste. From Fourier transform infrared spectroscopy and thermogravimetric analysis coupled with mass spectroscopy time-series measurements, it was found that powdered AAS was largely carbonated within 28 days with a CO₂ uptake of 14 wt%. The main carbonation products were calcium carbonates. Nevertheless, the bulk paste samples were highly resistant to carbonation, regardless of the exposure conditions. The findings showed that the pH value (initial pH > 12) and strength of the samples did not decrease under accelerated carbonation compared to those of the samples exposed under natural conditions. The mineralogy of the samples in these two carbonation exposures did not alter either, except for outdoor conditions. The gel pores were dominant in the pastes (pore size in range of 2–15 nm). The dense microstructure was the main barrier for CO₂ to diffuse and further react with binding phases.

Keywords AAS · Carbonation · TG-MS · pH · Gel porosity

Introduction

Ground granulated blast furnace slag (GGBFS) is a byproduct from steel production that has been widely used as a supplementary cementitious material (SCM) in blended cements [1]. In the Netherlands, the building industry has almost a century of experience in the use of GGBFS cements with a high GGBFS content, comparable to the current CEM III/B (66–80% GGBFS) as defined in EN 197-1 (2011) for major infrastructure, including marine concrete [2].

The binders with higher replacement such as above 70 wt% of GGBFS, have a significantly lower amount of calcium hydroxide (CH) than that in the ordinary Portland cement (OPC)-based binders [3]. Consequently, the faster carbonation of calcium silicate hydrate (C–S–H) gel occurs in GGBFS-based binders [4, 5]. Therefore, there is a certain level of OPC replacement by GGBFS (not more than 70 wt%), for which properties such as high mechanical strength and carbonation resistance still can be obtained [6]. On the other hand, the GGBFS valorization in the building industry can be achieved due to alkaline activation technology. The need for compelling utilization of byproducts and recovered waste materials, based on economic and environmental concerns, has led to the development of alkali-activated materials (AAMs). Alkali-activated slag (AAS) has been recognized for decades [7] as an environmentally friendly alternative to OPC based on two aspects. The first is the use of byproducts instead of natural resources for synthesis of AAS [8] and the second is its comparable or even better short and long-term properties compared to the OPC-based binders [9].

However, durability of AAS-based systems is still under debate, which limits their application in engineering

The contributing editor for this article was João António Labrincha Batista.

✉ Marija Nedeljković
M.Nedeljkovic@tudelft.nl

¹ Microlab, Faculty of Civil Engineering and Geosciences, Delft University of Technology, Stevinweg 1, 2628 CN Delft, The Netherlands

² Delta Concrete Consult BV & Nebest Adviesgroep, Marconiweg 2, 4131 PD Vianen, The Netherlands

practice. In particular, carbonation is of great interest since it induces both chemical and physical changes. It leads to corrosion of the steel reinforcement such as in OPC-based concrete. Namely, the corrosion of the steel reinforcement is inhibited due to the protective oxide film on the surface of the steel which is chemically stable in an alkaline concrete pore solution ($\text{pH} > 12.5$) [10]. However, the oxide film can be destroyed if the alkalinity of the pore solution drops. The CH buffers pH of the pore solution in OPC-based concrete, and it is consumed during the carbonation reaction with environmental CO_2 . As a result, the pH of the concrete pore solution drops from approximately 12.5 to < 9 [10]. If the carbonation front reaches the reinforcement and there is sufficient moisture around the steel reinforcement surface, the corrosion is likely to be initiated, limiting the service-life of concrete.

Researchers have been using different binder systems (AAS, and alkali-activated blended systems of GGBFS with fly ash or metakaoline) and exposures (CO_2 , RH) to study the carbonation mechanism of AAS in laboratory conditions [11–16]. On the other hand, the long-term properties of AAS binders in service conditions are rarely reported. For instance, Shi et al. [17] have presented a significant number of real applications of AAS concrete, however, the information about their long-term performance was limited. Xu et al. [18] by mechanical tests' results and microstructural characterization of the AAS concretes (activated by carbonates or carbonate/hydroxide solutions and cast between 1964 and 1982), demonstrated that the AAS concretes have served for prolonged periods, and their strength increased with time. Another study [16] showed that accelerated carbonation conditions did not replicate the carbonation rate in AAS concretes under natural conditions. Namely, lower carbonation depth was observed in AAS concrete in natural carbonation conditions after 7 years of exposure (with RH varying between 70 and 76% and temperature between 19 and 38 °C) compared to the predicted carbonation depth in accelerated carbonation conditions (1% v/v CO_2).

Contrary to excellent performance of AAS concrete in service, researchers have observed low carbonation resistance of AAS pastes, mortars and concretes in laboratory conditions [11, 19, 20]. To study the carbonation mechanism in AAS, generally pastes were ground to a fine powder and as such exposed to different carbonation conditions. In such a way more reaction sites would be provided for carbonation reaction. In all studies, it was found that AAS was carbonated regardless of the type and concentration of activator and exposure conditions. Furthermore, the carbonation resistance of AAS was found to be lower than that of OPC [19].

The general carbonation mechanism in AAS appears to be relatively well established by Bernal et al. [14, 21].

First, the carbonation of pore solution leads to the formation of sodium carbonates, followed by decalcification of C–(N)–A–S–H gel and consequent decay of mechanical strength of the AAS systems. A detailed study by Bernal et al. [21] on the effect of binder content on the performance of AAS concretes revealed that carbonation of the concrete mixtures with GGBFS content 400 kg/m^3 or higher is initially a chemically controlled process [22] followed by diffusion. When the carbonation depth becomes greater (more than 20% of the total examined depth), it was observed that diffusion of dissolved CO_2 through the pore network of the carbonated layer becomes dominant in determining the rate of further carbonation. It was also found that the use of higher binder content ($400\text{--}500 \text{ kg/m}^3$) resulted in a reduction of carbonation depth of AAS concretes. Furthermore, Bernal et al. [13] found that beside binder content, the binder chemistry significantly influences carbonation rate, in particular MgO content of raw GGBFS. Hydrotalcite-like phases (Mg–Al layered double hydroxides) have been seen to increase the resistance to carbonation of alkali-silicate activated GGBFS by absorbing CO_2 in their structure [13]. However, when GGBFS is blended with other precursors such as fly ash or metakaolin [11, 12, 15], these systems exhibited lower resistance to accelerated carbonation compared to pure AAS systems due to their different pore solution chemistry [14] and composition of the precursors.

Although the studies on powdered pastes are of immense value in understanding the carbonation mechanism in the AAS, the effect of carbonation on pore structure and mechanical properties cannot be then captured at the powdered paste level. Pore structure is the most fundamental paste property. Grinding eliminates much of the capillary porosity and this removes the mechanism that collapses the large gel pores [23]. Any diffusion mechanism occurring in the porous media is directly or indirectly controlled by its pore structure. The influence of the pore structure of AAS bulk paste on the carbonation rate was barely discussed in the literature regarding CO_2 diffusion path.

Therefore, the aim of this paper is twofold: (i) to study carbonation of powdered AAS pastes, with a focus on reactivity of CO_2 and maximum CO_2 uptake, and (ii) to investigate carbonation of bulk AAS pastes in terms of reactivity but also diffusivity of CO_2 , while capturing the effect of chemical degradation on the pore structure and mechanical properties, which is not possible within the first part. In this way, the paper may provide fundamental insight on the role of pore structure, and exposure conditions, such as relative humidity (RH) and CO_2 concentration on the carbonation mechanism at the paste level.

Materials and Sample Preparation

The GGBFS used in this study was supplied by ORCEM (the Netherlands). X-ray fluorescence (XRF) measurements were carried out using a PANalytical's Epsilon 3^{XLE} spectrometer equipped with a Rhodium X-ray source, the silicon-drift detector with 135 eV resolution at 5.9 keV/1000 cps. A 2–3 g of GGBFS powder was poured in a 32-mm spectro cup fitted with a bottom of stretched 4- μm prolene film held with a concentric ring. The chemical composition of the GGBFS determined by XRF is given in Table 1. The negative LOI value was related to the oxidation of sulfur-rich species in the GGBFS. It should be noted that the GGBFS was heated to 950 °C in air to determine the LOI, which was not corrected in the XRF measurements.

Figure 1 shows the particle size distribution of GGBFS, which was measured by laser diffraction analyzer. The instrument can provide particle size distribution ranging from 0.1 to 1000 μm . The chosen dispersant was ethanol. An external ultrasonic bath was used for de-agglomeration of the GGBFS particles. The average particle size of GGBFS, d_{50} , was 19 μm .

The X-ray diffractogram (XRD) of GGBFS was performed using a Philips PW 1830 powder X-ray diffractometer, with Co $K\alpha$ (1.789 Å) radiation, tube setting 40 kV and 40 mA, a step size of 0.030°, a rate of 2.0 s per step and a 2 Theta range of 10°–70°. The amorphous phase was dominant (Fig. 2).

The alkaline activator was prepared by mixing anhydrous pellets of sodium hydroxide with deionized water and commercial sodium silicate solution (27.5 wt% SiO_2 , 8.25 wt% Na_2O). The sodium silicate modulus i.e. $\text{SiO}_2/\text{Na}_2\text{O}$ mass ratio of the activator prepared and used for alkali activation was 1.5. The liquid-to-GGBFS ratio was 0.5. The liquid includes the solid part of the activator as well. After mixing, the activator was cooled down at room temperature for 24 h prior to the preparation of the pastes.

Before the preparation of paste samples for the carbonation study, the appearance of cracking and compressive strength was monitored at the certain curing age on prismatic AAS paste samples (160 × 40 × 40 mm³) according to the NEN-EN 196-1. The test was carried out because of the sensitivity of AAS pastes to drying and autogenous shrinkage reported by a previous study [24]. Two groups of samples were investigated, unsealed and sealed prismatic samples. The specific aim of the test was to obtain sufficient curing time and avoid shrinkage cracks. The cracks can ultimately underestimate compressive

strength of the samples at the later ages, when coupled effect of drying shrinkage and carbonation exposure on results of compressive strength would be difficult to interpret. Therefore, the samples were cured for 7, 14, 18, 21, 28, and 40 days. After each curing period, the samples were moved from the fog room to the laboratory conditions at 20 °C and 55% RH. The cracks were observed after each curing age in the laboratory conditions, except for the 28-day-cured samples for both, unsealed (Fig. 3) and sealed samples (not shown in this study). At 28 days, the samples did not have any crack, nor did the samples after 40 days of curing, which was the extended curing time to ensure that even after 28 days, no cracking would appear.

At 40 days, compressive strengths of all samples (with different curing durations within 40 days) were tested. For each curing regime, three samples were tested. The results are presented in Fig. 4. It can be seen that compressive strength did not increase significantly beyond 14 days of curing in the fog room. However, the drying shrinkage cracks were observed on the samples with curing time less than 28 days. Although cracking did not affect compressive strength results, these cracks could enable faster gas and water penetration into the samples, thereby reducing the durability of the material. Therefore, all samples for the carbonation study were cured for 28 days. The compressive strength during curing and preconditioning of AAS paste samples, as after different carbonation time exposures, was also examined in the last section of this study for unsealed cured samples.

The curing regime for the paste samples for carbonation study, i.e. 28 days in a fog room and then 28 days of

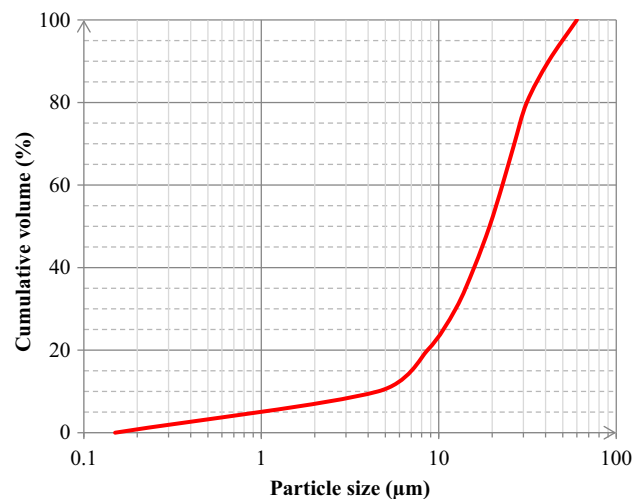


Fig. 1 Particle size distribution of GGBFS (Color figure online)

Table 1 Chemical composition of raw GGBFS measured by XRF

	SiO_2	Al_2O_3	CaO	MgO	Fe_2O_3	S	Na_2O	K_2O	TiO_2	L.O.I.
GGBFS	35.50	13.50	39.80	8.00	0.64	1.04	0.40	0.53	1.00	−1.30

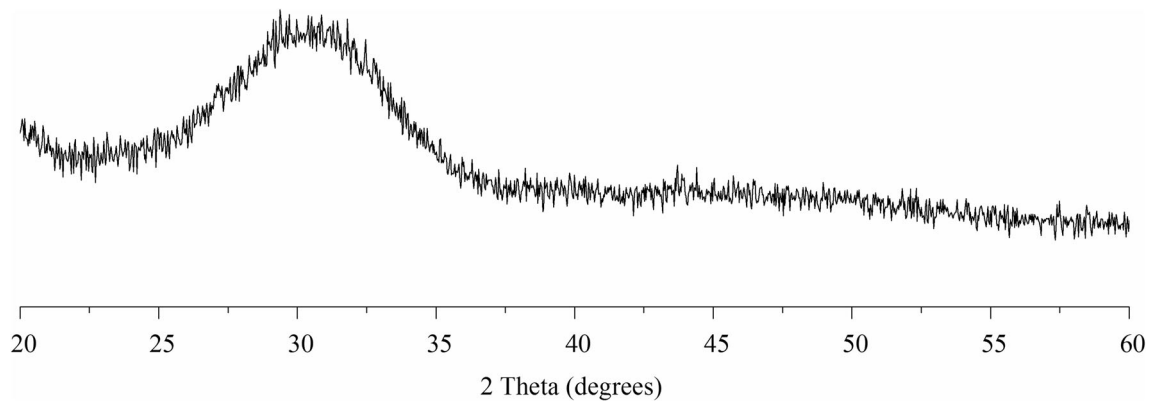
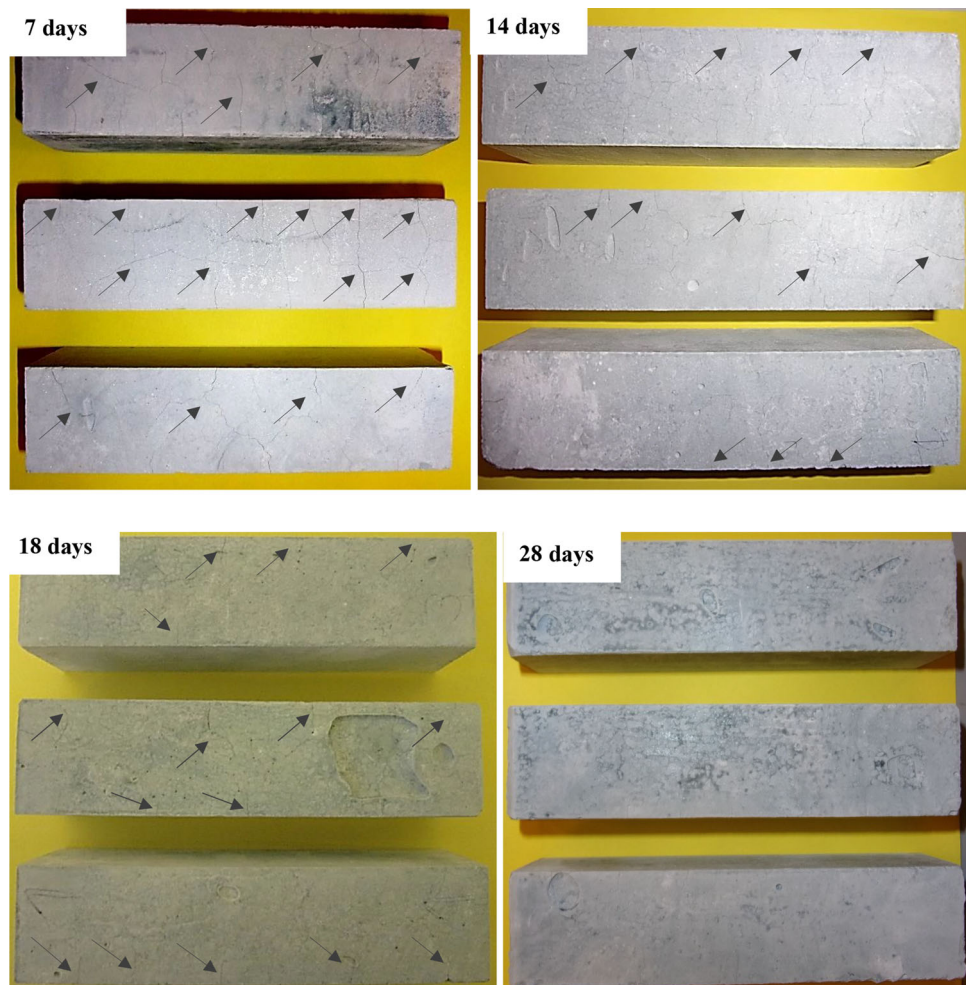


Fig. 2 XRD diffractogram of GGBFS

Fig. 3 Direct observations of cured samples surface for 7, 14, 18, 28 days. Arrows point to cracks. (The cracks were the most present on the top surface, while on the other sides of samples their appearance was less) (Color figure online)



preconditioning in the laboratory conditions, was chosen after a study on prismatic samples. The purpose of samples preconditioning in the laboratory conditions for an additional 28 days was to obtain nonsaturated conditions, so that the pores of the samples are partially filled with the moisture and that CO_2 molecules can diffuse. The pastes for the carbonation study were cast in cylinders with

54 mm diameter and height of 100 mm. The samples were sealed and cured for 28 days. The sealing of the samples was applied to prevent premature carbonation.

Figure 5 shows typical cylindric paste sample after 28 days of sealed curing. The cylindric samples were further placed in the laboratory conditions at 20 °C and 55% RH for additional 28 days (preconditioning of the

samples). At the age of 56 days, the samples were exposed to different environmental conditions as described in Table 2. It should be noted that one group of the samples was sealed cured for one year (reference, noncarbonated samples) to provide a baseline for comparison with carbonated samples at the end of the carbonation exposure.

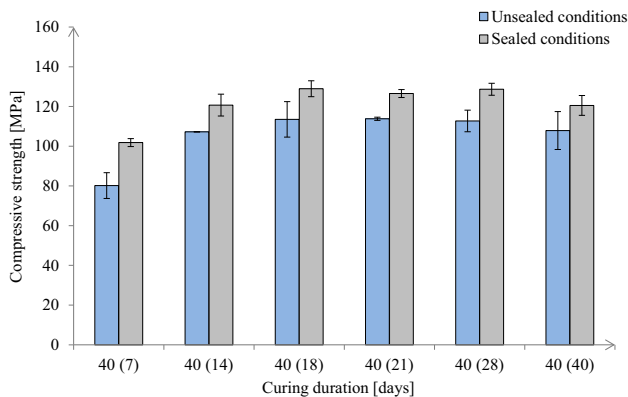


Fig. 4 At 40 days compressive strengths of the samples with different curing durations [For instance, 40 (7) means that sample was cured 7 days in the fog room (blue-colored columns), or foil sealed cured (gray-colored columns) and from 7 to 40 days was unsealed cured in natural laboratory conditions] (Color figure online)

Experimental Program

Samples were divided into two groups (Table 3, Fig. 5). The first group of pastes was crushed and ground to a powder with an average particle size $< 75 \mu\text{m}$ and exposed to accelerated conditions, 1% v/v CO_2 , 60% RH. The average particle size of $75 \mu\text{m}$ was adopted in this study according to the literature [11, 12, 25], where this size was used or it was shown that it is the one providing the full carbonation in a practical timescale. The second group of the samples was of initial cylindrical form (bulk samples) and as such was exposed to different conditions as described in Table 2.

Carbonation capacity, carbonation products, and CO_2 uptake in powdered pastes, were studied with Fourier transform infrared spectroscopy (FT-IR), X-ray diffraction (XRD), thermogravimetric analysis coupled with mass spectroscopy (TG-MS), respectively. The powdered paste samples were exposed in a climate chamber with 1% v/v CO_2 concentration, 60% RH, and 20°C . It should be noted that the powdered samples with regard to carbonation capacity testing were analyzed without any defined predrying, while for all other tests samples were prepared as described later. The bulk AAS pastes were exposed in natural [laboratory and outdoor (unsheltered)] and accelerated carbonation conditions (Table 2). In addition to FT-IR, XRD, TG-MS study, pore solution analysis enabled pH measurements and quantitation of the main present ions



Fig. 5 Bulk sample after demolding (left), and ground sample (right) (Color figure online)

Table 2 Exposure conditions

	Natural laboratory	Natural outdoor	Accelerated carbonation
CO_2 concentration	0.04% v/v	0.04% v/v	1% v/v
Relative humidity	50–60%	80–98%	60%
Temperature	20°C	$0\text{--}20^\circ\text{C}$	20°C

Table 3 Methodology

Crushed pastes (powder)		Reaction products
FT-IR, XRD, TG-MS		
Bulk pastes	Reaction products	Pore solution
	FT-IR, XRD, TG-MS, ESEM, N ₂	Pore solution composition, pH

(Na⁺, K⁺, Ca²⁺) in bulk paste samples. Nitrogen-adsorption (N₂-adsorption), ESEM, and compressive strength tests were used to study effects of different carbonation conditions on pore structure and mechanical properties of bulk paste samples.

The silicate and carbonate chemical bands were identified in powdered pastes at different time intervals by attenuated total reflectance Fourier transformed infrared spectroscopy (FT-IR). Spectra were acquired using PerkinElmer Spectrum 100, over the wavelength range of 2000–600 cm⁻¹ with a resolution of 4 cm⁻¹. A total of 16 scans were collected per measurement.

For XRD phase identification, the representative samples were gently crushed and then immersed in isopropanol for 1 week, by which period water is first replaced and then evaporated. Subsequently, samples were placed under vacuum at 25 °C for a minimum of 3 weeks. XRD measurements were carried out using Philips PW 1830 powder X-ray diffractometer equipped with X'pert High Score Plus software.

Thermogravimetric (TG) analysis was carried out using a heating rate of 10 °C/min between 40 and 1000 °C, with an argon purge at 70 ml/min. The sample predrying preparation was done in the same way as for XRD analysis. The thermobalance Netzsch STA 449 F3 Jupiter was coupled with a mass spectrometer (MS) Netzsch QMS 403 C, to identify more accurately the temperature range of H₂O and CO₂ emissions and to quantitate CO₂ uptake. The well-dried samples were ground into powder. The mass of powdered samples for testing was approximately 35 mg.

The microstructure of the samples from 56 days and 1 year of exposure was studied by ESEM. Similar to XRD analysis, the reaction of the pastes was stopped using isopropanol. The samples were crushed into small pieces with dimensions of 1–2 cm³ and impregnated using a low-viscosity epoxy resin and polished down to ¼ µm.

The internal RH of bulk AAS pastes was measured by Rotronic HygroLab C1 equipped with two HC2-AW RH station probes with an accuracy ± 1% RH. The samples were crashed in small pieces, and only core sample pieces were put in two plastic containers, in the measuring

chambers. Before the measurements, RH probes were calibrated using saturated salt solutions with known constant RH in the range of 65–95%. More detailed information about the internal RH measurement procedure can be found in the study of Huang and Ye [26]. The RH was measured at 28 days, and for all exposure conditions at 1 year.

The procedure for pore solution extraction from AAS pastes is adopted from [27]. Pressures of up to 750 MPa were used to extract pore fluid from the samples. The cylindrical paste samples with 35 mm diameter and 70 mm height were used for pore solution extraction. After extraction, the pore solution was filtered and half of each solution was diluted using nitric acid (0.2 vol%). The diluted solutions were analyzed in a Perkin Elmer Optima 5300 DV apparatus. The nondiluted solutions were left for measurement of OH⁻ concentration in the pore solution by titration against HCl acid.

It should be noted that it was not possible to obtain a sufficient amount of pore solution in all cases. In samples with sufficient extracted volume of pore solution, pH was determined through measurement of OH⁻ concentration. For samples where this was not the case, the pH measurements were carried out on the simulated pore solution, by dissolving 1 g of powdered sample in 10 ml of deionized water. The suspension was magnet rotated and maintained during 15 min at ambient temperature. Subsequently, the pH of pore solution was measured by pH meter 827 Metrohm. To verify the suspension method, samples with sufficient extracted pore solution for analysis were also ground into powder and mixed with water to obtain suspension and measure their pH. This way, the suspension method was shown to be a good indicator of the pH value, in addition to the standard method (i.e. analysis of the extracted pore solution).

The sample preparation for N₂ adsorption was the same as for ESEM analysis with the exception that samples were not impregnated, instead they were weighed and degassed under vacuum at 25 °C. Approximately 1 g of sample was used for the analysis. The N₂-adsorption tests were conducted by using Gemini VII 2390 with a relative pressure P/P_0 range from 0.05 to 0.99 (the relative pressure is defined as the equilibrium vapor pressure divided by the saturation vapor pressure). A relative pressure of 0.99 corresponds to a pore-size of 193.5 nm, which is a maximum pore size that can be assessed. The volumetric method was used to determine the molar quantity of nitrogen adsorbed on hardened AAS pastes from the pressure and temperature measurement, using the real gas equation of state. The Brunauer–Emmett–Teller (BET) [28] gas-adsorption method has been applied for determination of the surface area of samples. The pore size distribution is obtained by Barrett–Joyner–Halenda (BJH)

technique [29], assuming cylindrical, nonconnecting pore geometry.

Results and Discussion

Carbonation of Powdered Pastes

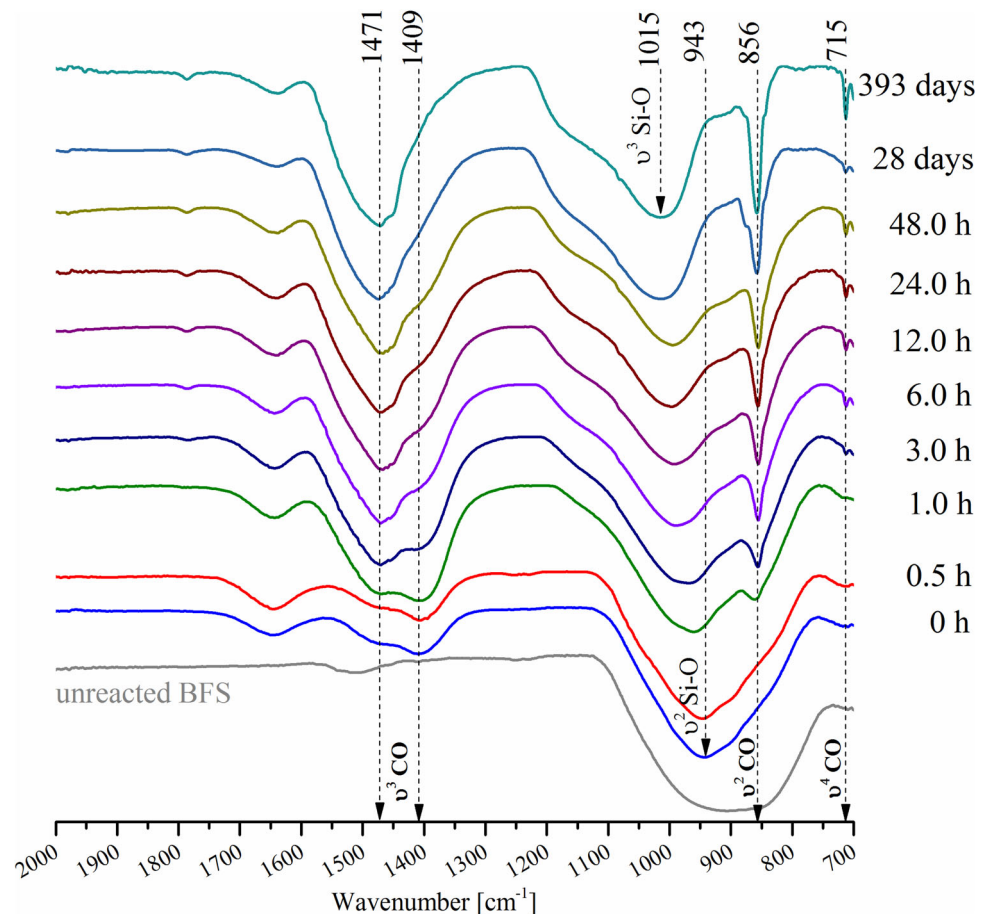
FT-IR Study

Figure 6 compares several FT-IR spectra; of unreacted GGBFS, reference AAS (0 h) and spectra of carbonated AAS pastes. In general, the Si–O–Si stretching vibrations for the SiQⁿ units in glasses show infrared absorption bands in the domain 850–1200 cm⁻¹ [30, 31]. The broad band region for unreacted GGBFS at 900 cm⁻¹ indicates general disorder in the silicate network reflecting the wide distribution of Qⁿ units in an amorphous GGBFS. On the other hand, FT-IR spectrum of AAS (0 h) shows that the main band shifts to a higher wavenumber at 943 cm⁻¹ as a result of alkali activation of GGBFS and formation of C–(N–)A–S–H gel. The broad and weak shoulder at 710–715 cm⁻¹ can be observed at $t = 0$ for AAS paste which is assigned

to the bending of Al–O–Si bands in ring structures consistent with the study of Bernal et al. [32]. This band also appears in unreacted GGBFS (Fig. 6).

The effect of accelerated carbonation on the local bonding environment in AAS powdered paste is shown also in Fig. 6. The AAS paste was ground to provide more reaction sites on a well distributed surface grain area of the paste powder. The FT-IR has different vibrational bands for carbonates due to their different local bonding environment [14]. They are marked in Fig. 6 as: ν^3 CO for asymmetric stretching vibration of carbonates, ν^2 CO for out of plane bending vibration of carbonates, ν^4 CO for in plane bending vibration of bicarbonates, centered at 1471, 856 and 715 cm⁻¹, respectively. These bands correspond to calcium carbonates, aragonite and calcite, with an exception that band at 715 cm⁻¹ can correspond also to the bending of Al–O–Si bands as observed for noncarbonated powder. The first significant change between reference and carbonated powder can be seen after 1 h of carbonation exposure. The peak at 856 cm⁻¹ is formed and its intensity increases with longer exposure. The shoulder at ~ 840 cm⁻¹ in the carbonated samples can be also observed. This band can be assigned to a bending mode in

Fig. 6 FT-IR spectra of powdered AAS exposed to accelerated carbonation (Color figure online)



the HCO_3^- ion [11]. The Si–O–T (with T = Al, Si) band shifts from lower toward higher wavenumbers ($943 \rightarrow 1015 \text{ cm}^{-1}$). This indicates polymerization of silicate gel due to decalcification of the main reaction product of AAS paste, C–(N–)A–S–H gel, such as found by Bernal et al. [11]. The $\nu^3 \text{CO}$ band centered at 1471 cm^{-1} and Si–O–T band at 1015 cm^{-1} , did not change intensity after 393 days of exposure. However, intensity of the peaks at 715 and 856 cm^{-1} is more pronounced after 393 days, and the shoulder at 1409 cm^{-1} disappeared.

XRD Study

Figure 7 compares XRD diffractograms of the reference raw GGBFS and the carbonated raw GGBFS. The reference sample is fully amorphous with regard to the large diffuse diffraction peak centered at 30° 2 Theta, while the intensity of the same peak decreases in carbonated raw GGBFS. It seems that carbonation suppresses the amorphous phase in raw GGBFS. Nevertheless, no other phases were formed, suggesting that raw GGBFS is inert to carbonation.

Figure 8 compares the XRD diffractograms of reference and carbonated powdered AAS paste after 28 days of accelerated carbonation. The powdered AAS paste shows no crystalline phases, compared to carbonated powdered paste in which two different types of carbonates, sodium-based and calcium-based carbonates were identified. Nahcolite (NaHCO_3) and gaylussite ($\text{Na}_2\text{Ca}(\text{CO}_3)_2 \cdot 5\text{H}_2\text{O}$) were identified as sodium-based carbonates, which originated from the carbonation of the Na^+ and Ca^{2+} ions from the aqueous solution. The identification of nahcolite is consistent with the FT-IR data (Fig. 6). The formation of aqueous solution may be favored in the accelerated carbonation environment between moisture, CO_2 molecules

and free alkalis from the powder surface. On the other hand, calcium carbonates, i.e. vaterite, aragonite and calcite were formed due to carbonation of C–(N–)A–S–H gel. Carbonation mechanism can be explained by the cation-exchanging reaction of Ca^{2+} from the gel inter- or sheet layers with H^+ or Na^+ from the aqueous solution. Subsequently, reaction of Ca^{2+} with CO_3^{2-} from aqueous solution results in calcium carbonates formation, when the solution is supersaturated with these species. Consequently, polymerization of decalcified gel occurs by condensation of neighboring groups Si–OH or Si–O–Na into silicate gel, as observed in FT-IR analyses. Carbonation products and CO_2 uptake were further studied by the TG-MS technique.

TG-MS Study

TG and MS results were combined to measure the maximum uptake of CO_2 from the carbonated powder. Considering both the MS curve for CO_2 and DTG curve (Fig. 9), the weight loss in the range of $230\text{--}730^\circ\text{C}$ is indicated as the temperature range for decomposition of metastable (low-crystalline) and stable calcium carbonates [33, 34] and this range was used for CO_2 uptake. The maximum CO_2 uptake was 14% by weight of dried powder, as calculated according to Taylor's method [35]. A similar value was reported for high strength Klockner Oxygen Blown Maxhutte steel slag binder activated by carbonation with a CO_2 uptake of 13% [36]. Furthermore, besides two sharp features in the MS curve, corresponding to different atomic structural forms of calcium carbonates present in the carbonated powder, one more carbonate phase can be observed at a very low temperature, a narrow shoulder around 140°C . The appearance of this shoulder in the MS curve indicates a rather low amount of this phase in carbonated powder, compared to calcium carbonates and

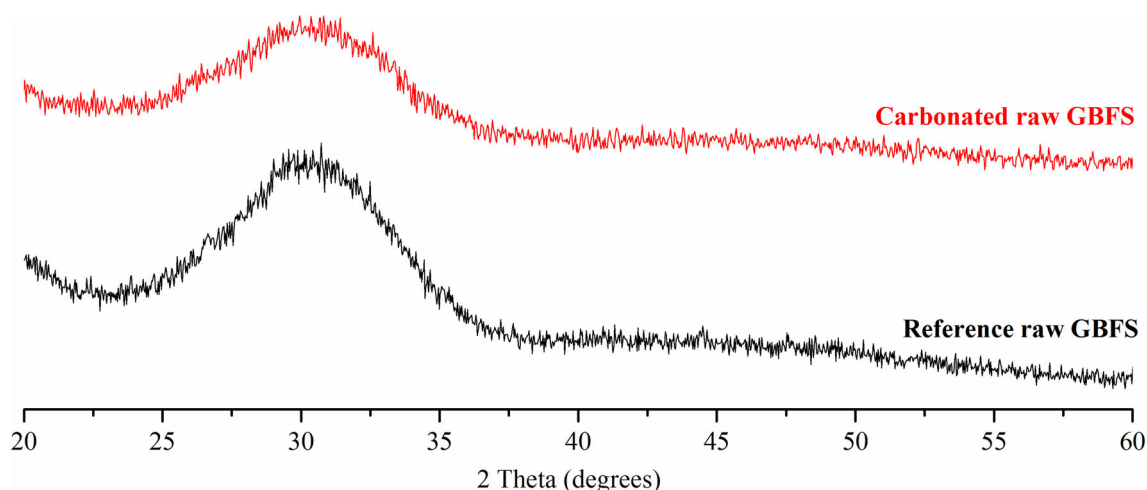


Fig. 7 XRD diffractograms of reference raw GGBFS and carbonated raw GGBFS after 28 days of exposure to 1% v/v CO_2 (Color figure online)

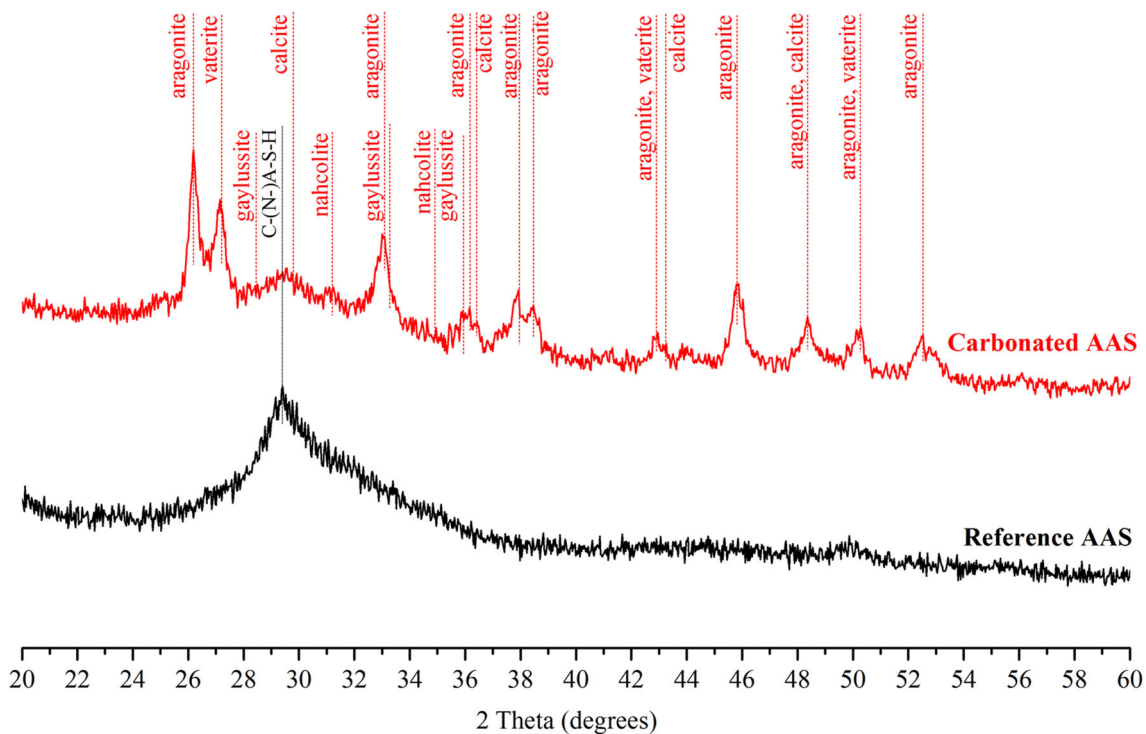


Fig. 8 XRD diffractograms of reference and carbonated powdered AAS pastes after 28 days of exposure to 1% v/v CO₂. Reference powder diffraction files (PDF#) from ICSD database: Nahcolite

(PDF# 15-700), Gaylussite (PDF# 21-343), Aragonite (PDF# 41-1475), Vaterite (PDF# 33-268), Calcite (PDF# 47-1743) (Color figure online)

therefore it was not included for calculation of the CO₂ uptake. It is believed that the present phase is nahcolite (NaHCO₃), which was previously identified by the XRD and FT-IR analysis.

Carbonation of Bulk Pastes

Pore Solution Study

The RH and pH measurements of the pastes in different exposures and time intervals are presented in Table 4. The internal RH results show that samples had 60–70% RH at which CO₂ diffusion is suggested to be the fastest [15], except for AAS that was exposed outdoor. In outdoor conditions, i.e. in climate conditions of the Netherlands, RH varies between 80 and 99% RH. Therefore, samples are expected to be saturated such as measured in this study (RH outdoor ~ 95%). However, wetting and drying of the samples during 1 year can provide perfect conditions for carbonation, which is reflected by element concentrations, primarily by reduction of Na⁺ and K⁺. From Table 4 it can be clearly seen that Na⁺ content was reduced 10 times, and so were other elements, except Fe. Considering that the samples were exposed in the outdoor (unsheltered) conditions, the loss of Na⁺ can also be attributed to the leaching of unbonded Na⁺.

Although the alkalis (Na⁺, K⁺, Ca²⁺) in the pore solution were reduced significantly, the pH did not drop below 11. The Na content obtained in outdoor exposed AAS was similar to Na content in noncarbonated GGBFS cements, such as found by Kempl and Çopuroğlu [27]. The corresponding pH value was above 12 in the noncarbonated GGBFS pastes. The minimum pH detected in natural outdoor conditions was 12.18. The high pH values, regardless of the pH measurement method, suggested strong alkaline media under all exposures after 1 year, indicating slightly carbonated or noncarbonated pore solution of AAS pastes.

FT-IR Study

FT-IR spectra of the bulk samples are presented in Fig. 10. After 1 year, peak locations for chemical bands of sealed and exposed AAS pastes were similar, suggesting no carbonation effect on the molecular structure of the gel, except for the samples that were exposed outdoor. The band at 1471 cm⁻¹ indicated the presence of carbonates, ν³ CO. However, this was a weak band compared to the bands of carbonates in spectra of powdered AAS (Fig. 6). In addition, the Si–O vibrational band also shifted to higher wavenumbers (943 → 957), indicating that the degree of silicon polymerization increased.

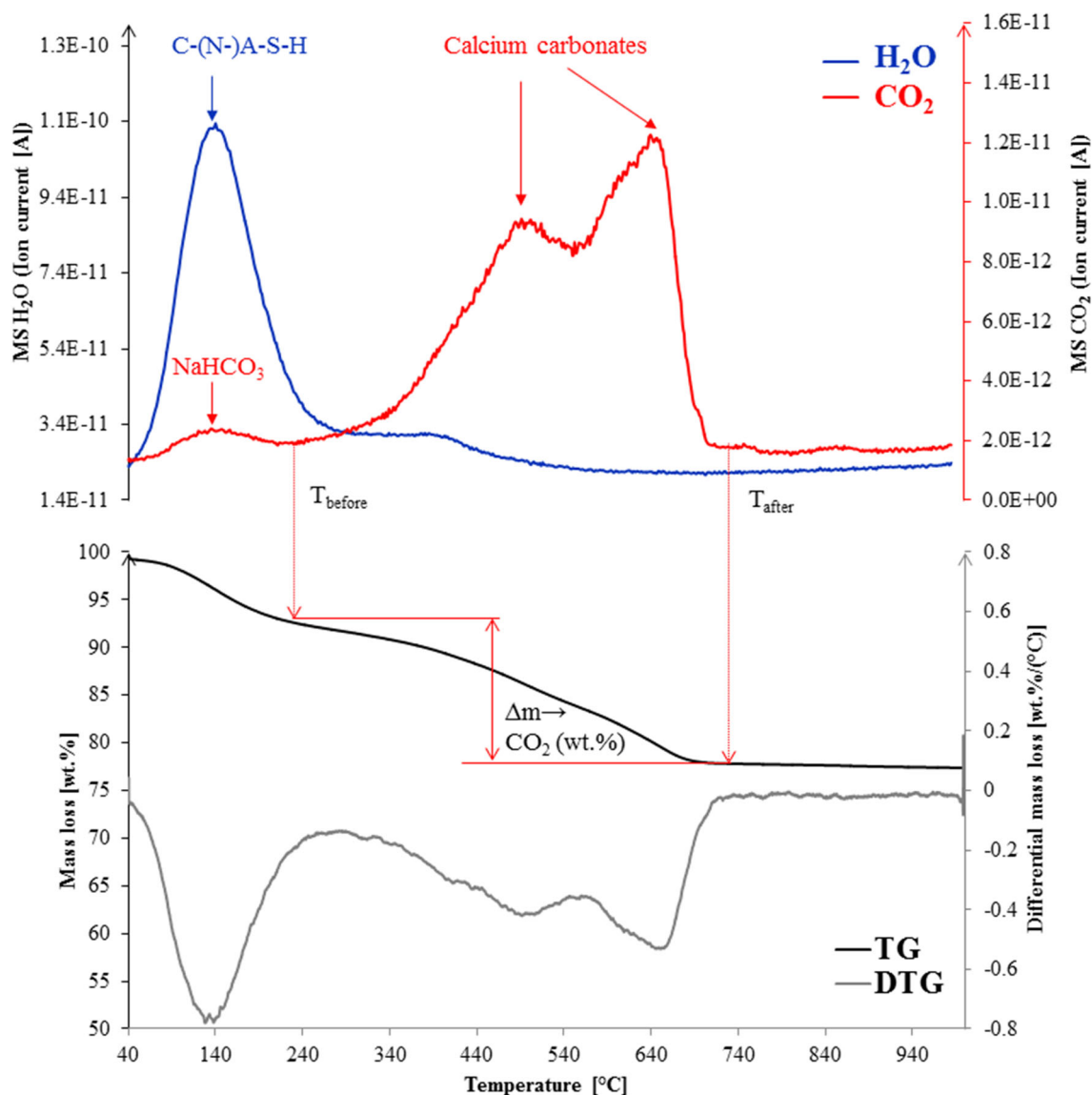


Fig. 9 TG-DTG-MS of a carbonated powdered AAS paste (Color figure online)

Table 4 RH-pH values and main element compositions of bulk AAS pastes pore solutions analyzed by ICP-OES

Sample	RH (%)	pH		Elemental composition of the pore solution					
		Standard method (-)	Suspension method (-)	[Na] (mmol/l)	[K]	[Mg]	[Ca]	[S]	[Fe]
AAS_28 d sealed	71.5	13.97	14.00	1555.22	35.65	8.35	29.50	573.14	0.30
AAS_393 d sealed	62.25	12.54	12.63	1570.22	43.25	7.86	31.28	766.59	0.16
AAS_393 d nat indoor	66.32	–	12.42	–	–	–	–	–	–
AAS_393 d nat outdoor	95.00	12.02	12.18	156.57	3.45	4.40	16.08	109.86	0.33

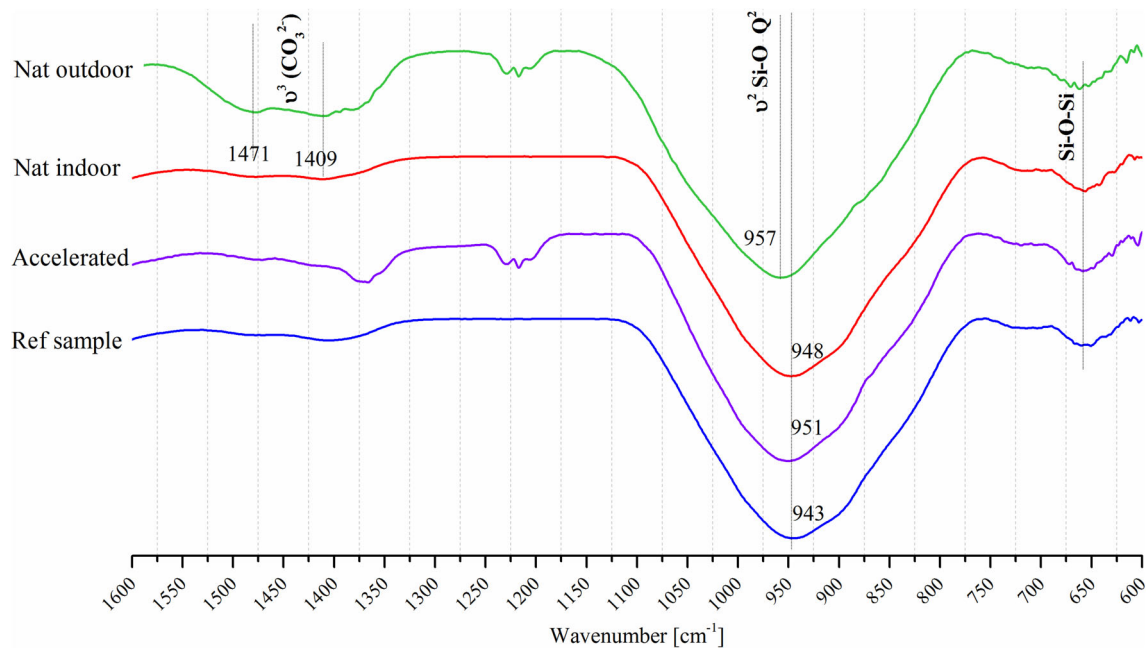


Fig. 10 FT-IR spectra of bulk AAS paste samples exposed to different environmental conditions (Color figure online)

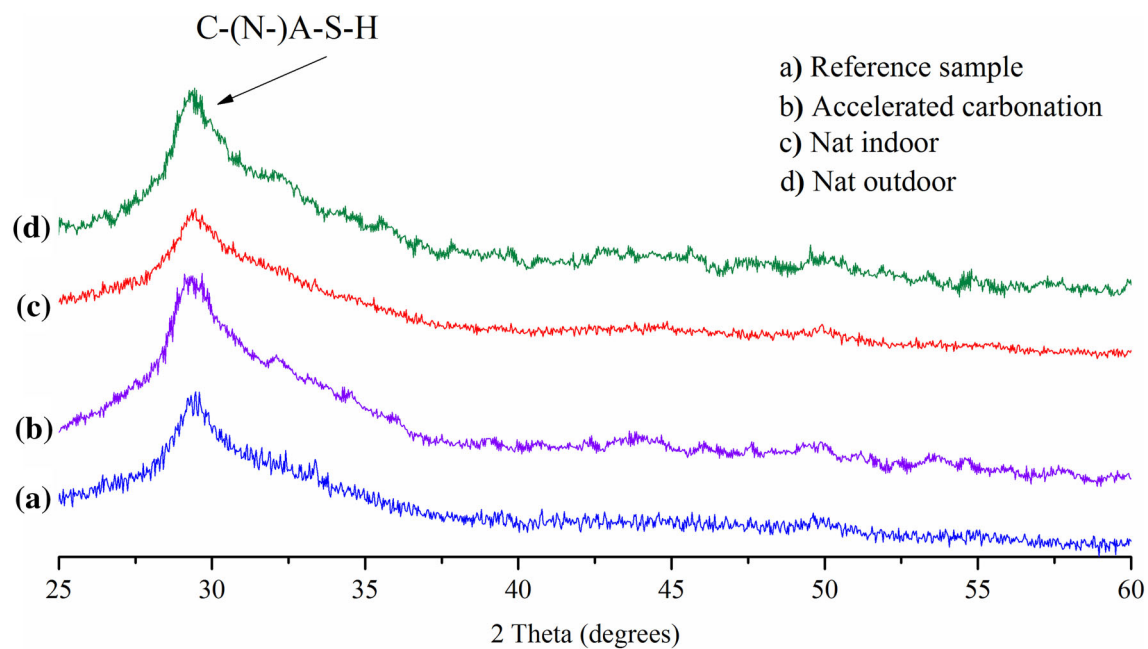


Fig. 11 XRD diffractograms of bulk AAS paste samples exposed to different environmental conditions (Color figure online)

XRD Study

Figure 11 shows the XRD diffractograms of bulk AAS pastes from all exposure conditions after 1 year. Comparing the features of the XRD diffractograms, there is no significant difference between reference and exposed samples. Carbonation of the C-(N-)A-S-H gel was equally limited in accelerated conditions. These results

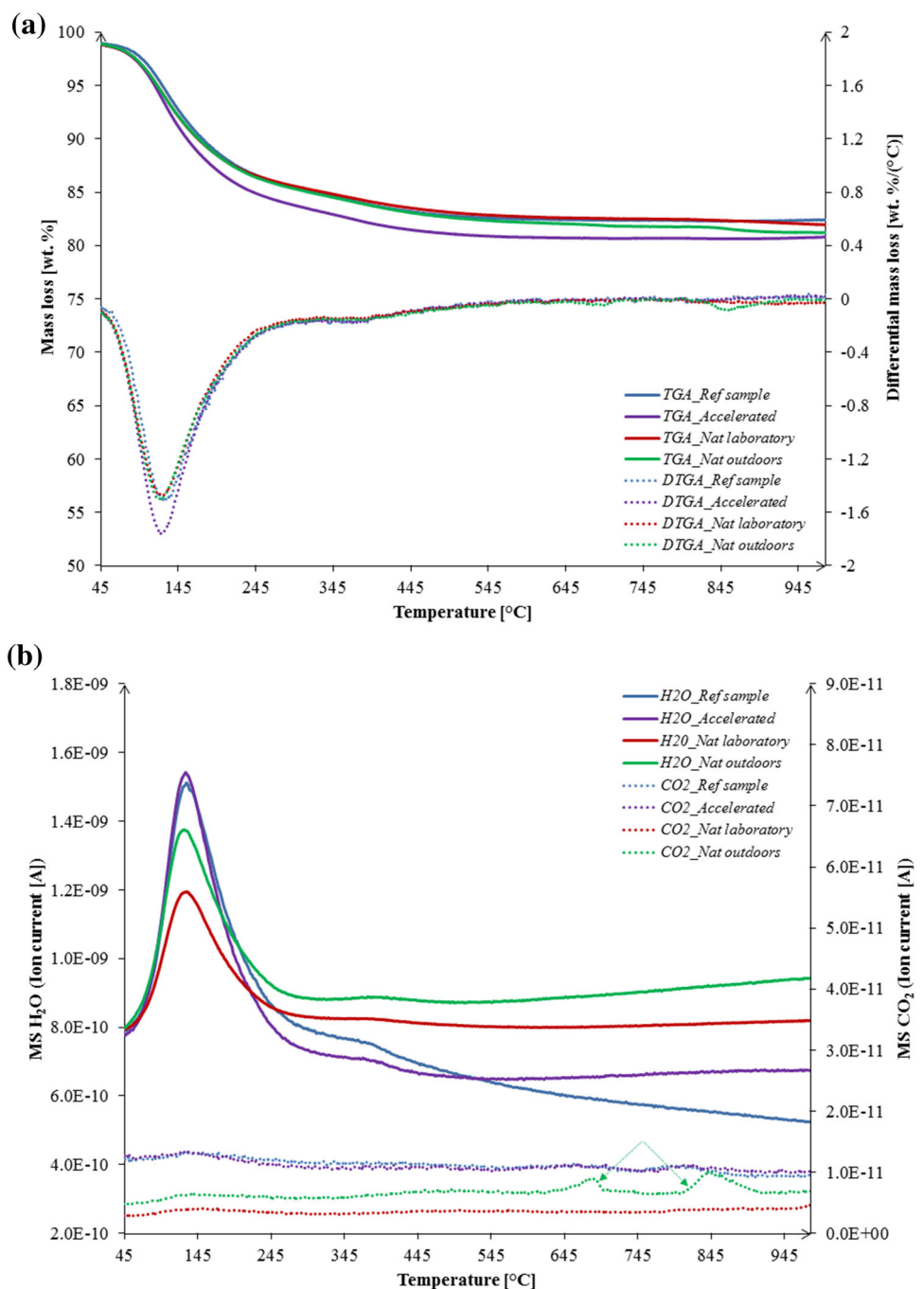
indicate that the material should be very dense, such that the pore sizes are close to molecular dimensions. These pores would then restrict CO₂ gas diffusion on the basis of their molecular dimensions rather than CO₂ molecular weight and concentration. This will be further discussed in the pore structure section.

TG-MS Study

The TG results combined with respective MS curves for release of H_2O and CO_2 are presented in Fig. 12a, b. The TG-DTG curves of all the pastes exhibited a one-stage thermal degradation process, suggesting a homogeneous reaction product (Fig. 12a). The mass loss at 105–345 °C corresponds to the emission of interlayer and chemically bound water from the C-(N-)A-S-H gel. From the TG

curves, the highest mass loss is measured in the conditions of accelerated carbonation. It is assumed that in these conditions gel was continuously developing due to the constant control of relative humidity value (Table 2). The MS curves clearly show that the release of water was dominant (Fig. 12b). Very little CO_2 was released for AAS paste in the natural outdoor conditions suggesting slight carbonation of the paste, as it was identified by FT-IR study.

Fig. 12 **a** TG-DTG curves for bulk AAS paste samples after 1 year in different exposure conditions. **b** MS curves for bulk AAS paste samples after 1 year in different exposure conditions (Color figure online)



Microstructure Study by ESEM

Figure 13 demonstrates microstructure morphology obtained by ESEM imaging. AAS pastes have similar microstructure either after 56 days of preconditioning or 1 year of natural laboratory carbonation where the gel is uniformly dispersed around the unreacted GGBFS particles. No evidence of carbonation was observed, which was confirmed by previous studies, such as with XRD study (Fig. 11). Similar microstructure was observed for water glass activated GGBFS containing 13.2% of MgO after 1 year by Haha et al. [37]. According to their results, such dense microstructure has very low porosity (max. 3 vol%) after 28 days of curing, which was also found in this study. Regarding microcracking of AAS such as often observed for dense and brittle materials, in this work no cracking was found, contrary to observations of Bernal et al. [13] and Brough et al. [38]. It can be concluded that the 28 days of sealed cured AAS pastes provided a volumetrically stable microstructural development.

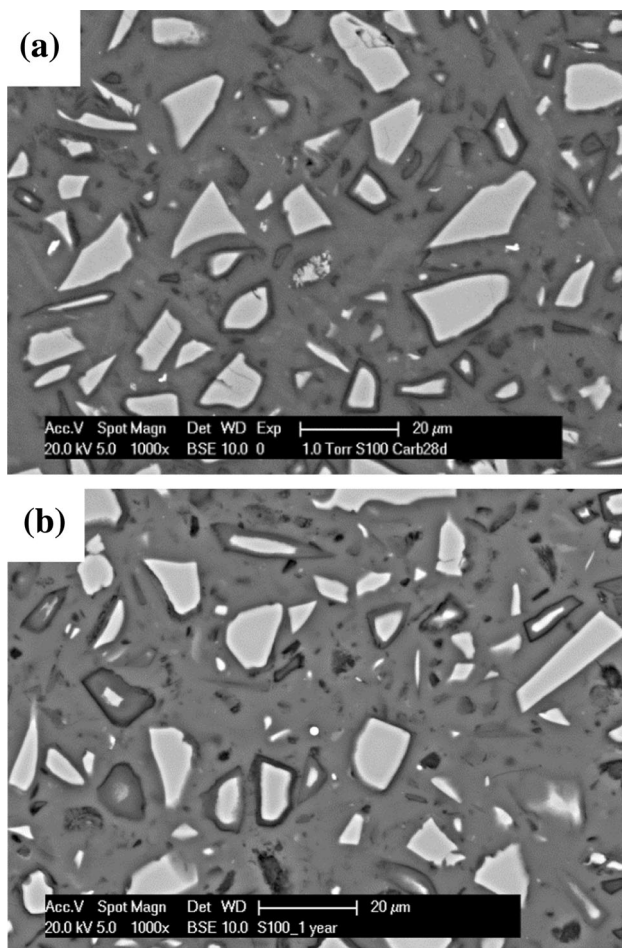


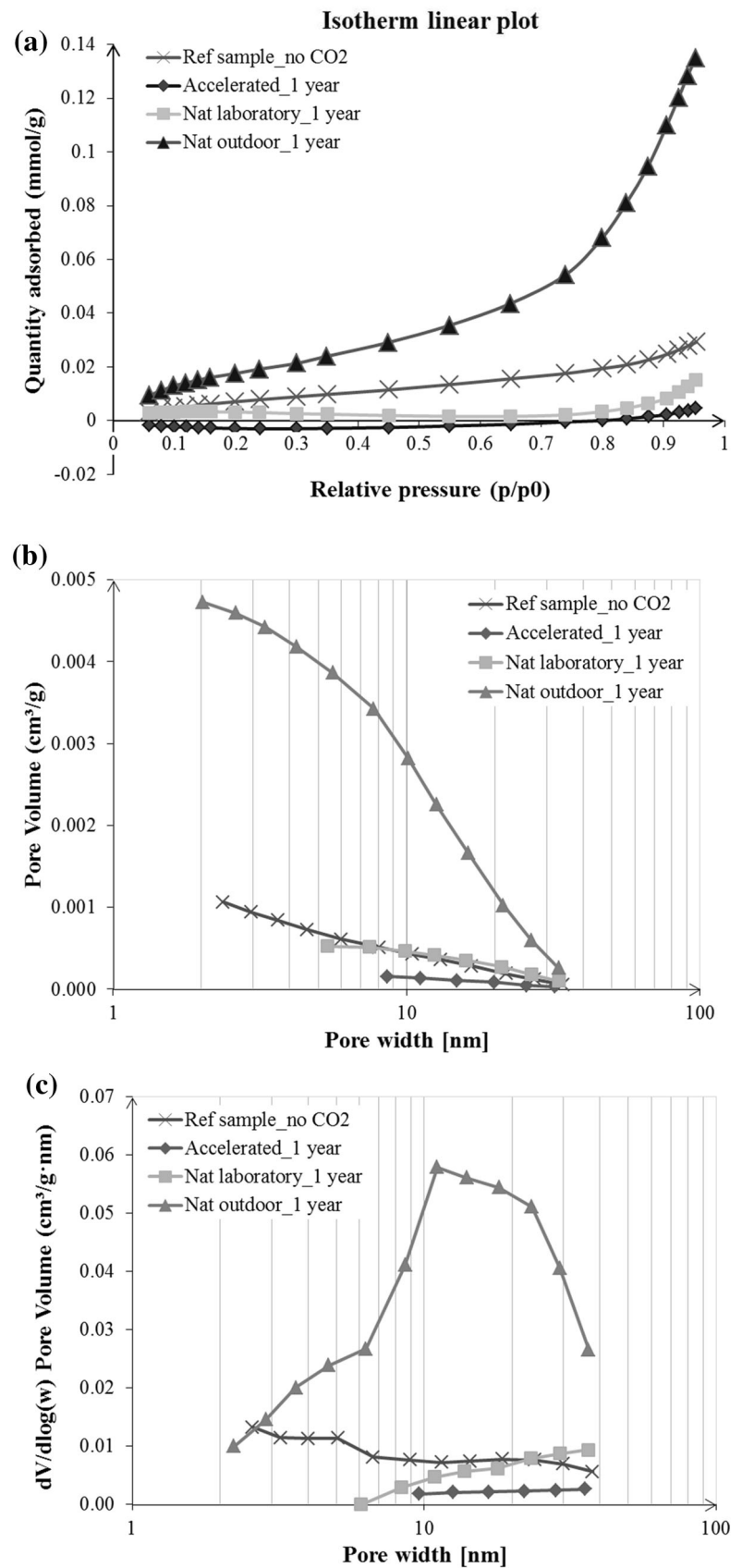
Fig. 13 ESEM-BSE images of bulk AAS paste samples after **a** 56 days of curing and preconditioning, **b** 1 year of exposure under natural laboratory conditions

Pore Structure Study by N₂ Adsorption

The pore structure was first tested by mercury intrusion porosimetry (MIP) method. The intrusion volume was extremely low so it was not possible to detect any characteristic pore diameter by MIP in AAS [39]. Therefore, N₂-adsorption technique was applied for pore structure analysis. Before considering pore size distribution, adsorption isotherms should be considered first. Figure 14a shows N₂-adsorption isotherms for four samples. The distinctive isotherm for the sample in the natural outdoor conditions has a steady increase in the adsorbed volume at approximately $p/p_0 = 0.4$ and a sharp increase in adsorbed volume from 0.4 to around $p/p_0 = 0.96$. The sharp increase is representative of bulk pore filling such as shown in [40]. Other curves indicated almost nonporous material property since the quantity of adsorbed N₂ was nearly 0.02 mmol/g. The shape of a N₂-adsorption isotherm can be used as a source of qualitative structural information to determine whether the pores present in the sample are micropores (below 2 nm), mesopores (between 2 and 50 nm), or macropores (above 50 nm) [41]. The isotherms in Fig. 14a are identified as slit-shaped pores according to the H3 type [41], similar to the synthesized C–S–H and montmorillonite isotherms identified in study by Costoya [42]. Comparison of the quantities of adsorbed N₂ between AAS paste in outdoor conditions (0.138 mmol/g) and for C₃S paste (~ 2 mmol/g) [42], indicated a much denser AAS paste microstructure as demonstrated by ESEM-BSE images (Fig. 13).

Converting the relative pressures (p/p_0) to pore diameters and obtaining the pore volume (Fig. 14b), it can be seen that a significantly higher volume is found for AAS in outdoor conditions ($5 \times 10^{-3} \text{ cm}^3/\text{g}$) compared to other exposures ($< 1 \times 10^{-3} \text{ cm}^3/\text{g}$). This can be due to more severe outdoor weathering of the material. The visually observed cracking of the samples, beside gel porosity, might contribute to pore volume increase. The BET_{N₂} surface areas of AAS in studied exposure conditions after 1 year follows the same trend as the pore volume change. The BET_{N₂} surface area of AAS in outdoor conditions (1.72 m²/g) was much higher than found for AAS in natural laboratory conditions (0.25 m²/g) or for the reference sample (0.79 m²/g). The pore structure study shows that the pore volumes measured in AAS pastes are far lower than the pore volumes normally found in OPC-GGBFS-based systems [34]. Furthermore, pore size distribution (PSD) is in the range of mesopores with diameter of 2 nm and maximum pore diameter of 15 nm, as shown in Fig. 14c. The transport mode for this range of pores sizes conforms Knudsen diffusion, according to Houst and Wittmann [43]. This means that the pore sizes are smaller

Fig. 14 a N_2 -adsorption isotherms for bulk AAS paste samples. **b** Pore volume of bulk AAS paste samples under different exposure conditions after 1 year. **c** PSD of bulk AAS paste samples under different exposure conditions after 1 year



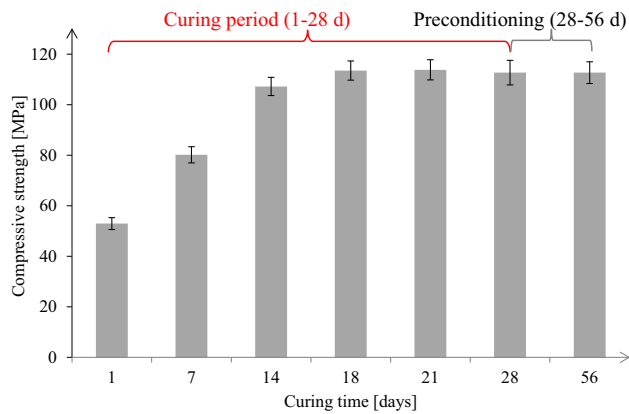


Fig. 15 Compressive strengths of bulk AAS paste samples during curing and preconditioning (Color figure online)

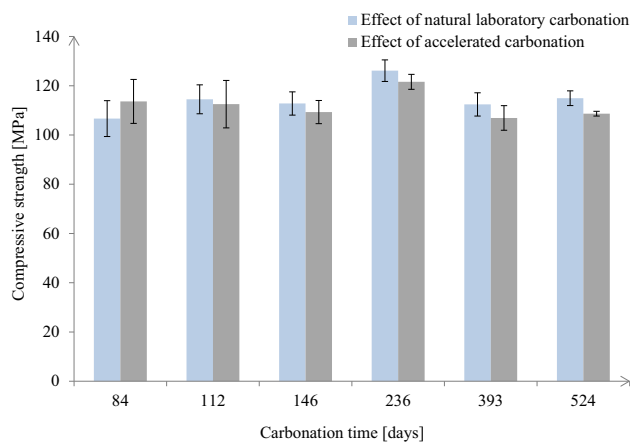


Fig. 16 Compressive strengths of bulk AAS paste samples during carbonation exposure (Color figure online)

than the mean free path of the gas molecules (O_2 or CO_2). Therefore, it is believed that accessible PSD is the main reason for carbonation resistance of AAS bulk paste samples in this study. Beside PSD, the transport of gases across the nanoporous material is also controlled by the pore connectivity [44]. In this regard, more fundamental insight using molecular level characterization techniques is needed to test the mode of CO_2 diffusion and interaction within such a dense system, such as in AAS.

Compressive Strength

Figure 15 presents compressive strength development in AAS during 56 days of curing and preconditioning. The results are higher than the results reported in previous studies [33, 34]. This is mainly due to the difference in alkaline solution composition (% Na_2O , SiO_2/Na_2O modulus ratio). The relatively low alkaline conditions used in this work (4.8% $Na_2O/100$ g of GGBFS compared to the 5, 10, 15 wt% Na_2O in [33]) provided effective dissolution of

GGBFS and formation of C-(N-)A-S-H gel, which is responsible for the strength gain. Furthermore, the results from this study suggested that the maximum compressive strength gain for AAS paste is relatively low beyond 14 days. An extended curing time in the fog room does not contribute to further increase of the compressive strength. In contrast, curing time for obtaining the maximum compressive strength in OPC-based paste is around 60 days, as reported by Chindaprasirt et al. [45]. The comparison is based on similar w/b ratio (0.35 for OPC-based paste and 0.38 for AAS paste).

Regarding the effect of carbonation on compressive strength, accelerated carbonation can decrease, but also it can increase compressive strength of AAS mortars, depending on the type of alkaline activator used and exposure conditions [15]. Figure 16 compares the compressive strength results of AAS paste samples exposed in natural laboratory and accelerated carbonation conditions. It can be seen that there is no significant difference in strength results from two different exposure conditions in this study.

Conclusions

Carbonation resistance of AAS under natural and accelerated conditions was evaluated. Two aspects were studied, the potential carbonation of the main binding phases in finely powdered paste and the reactivity and diffusivity of CO_2 within the bulk paste. In general, the carbonation of raw GGBFS was not possible, while carbonation of AAS powdered paste involves one reaction: the carbonation of gel (C-(N-)A-S-H). This reaction causes the gel decomposition and formation of different calcium carbonates. The majority of the CO_2 uptake was occurring within the first 28 days of accelerated carbonation. Nevertheless, the bulk samples were highly resistant to carbonation, regardless of the exposure conditions. Carbonation of bulk AAS pastes was inhibited due to their dense microstructure, the presence of extremely small pores with sizes ranging from sub-nanometers to tens of nanometers, and high alkalinity (pH values > 12.18). Nitrogen-adsorption tests identified the gel pores (< 15 nm) to be dominant in the system, which blocked CO_2 to diffuse into the pastes during the exposure period. The dense AAS microstructure exhibited high mechanical strength (~ 110 MPa). The results of this study shed light on the importance and the effects of the physical properties (density, pore size distribution) and alkalinity (pH) of AAS pastes on their long-term performance and durability.

Acknowledgements This research was carried out under the project S81.1.13498 within the framework of the Partnership Program of the

Materials innovation institute M2i (www.m2i.nl) and the Technology Foundation STW (www.stw.nl), which is part of the Netherlands Organisation for Scientific Research (www.nwo.nl). The authors gratefully acknowledge John van den Berg for his help with pore solution study.

Open Access This article is distributed under the terms of the Creative Commons Attribution 4.0 International License (<http://creativecommons.org/licenses/by/4.0/>), which permits unrestricted use, distribution, and reproduction in any medium, provided you give appropriate credit to the original author(s) and the source, provide a link to the Creative Commons license, and indicate if changes were made.

References

- Lothenbach B, Scrivener K, Hooton RD (2011) Supplementary cementitious materials. *Cem Concr Res* 41(12):1244–1256. <https://doi.org/10.1016/j.cemconres.2010.12.001>
- Polder RB, Nijland TG, de Rooij MR, Larsen CK, Pedersen B (2014) Innovation based on tradition: Blast furnace slag cement for durable concrete structures in Norway? In: Proceedings CIC2014 first concrete innovation conference, Oslo, Norway, 11–13 June 2014, pp 1–7
- Sisomphon K, Franke L (2011) Evaluation of calcium hydroxide contents in pozzolanic cement pastes by a chemical extraction method. *Constr Build Mater* 25(1):190–194. <https://doi.org/10.1016/j.conbuildmat.2010.06.039>
- Borges PH, Costa JO, Milestone NB, Lynsdale CJ, Streatfield RE (2010) Carbonation of CH and C–S–H in composite cement pastes containing high amounts of BFS. *Cem Concr Res* 40(2):284–292. <https://doi.org/10.1016/j.cemconres.2009.10.020>
- Gruyaert E, Van den Heede P, De Belie N (2013) Carbonation of slag concrete: effect of the cement replacement level and curing on the carbonation coefficient—effect of carbonation on the pore structure. *Cem Concr Compos* 35(1):39–48. <https://doi.org/10.1016/j.cemconcomp.2012.08.024>
- Holthuisen PE (2016) Chloride ingress of carbonated blast furnace slag cement mortars. Master's Thesis, Delft University of Technology, Delft, The Netherlands
- Davidovits J (1993) Geopolymer cements to minimise carbon-dioxide greenhouse-warming. *Ceram Trans* 37:165–182
- McLellan BC, Williams RP, Lay J, Van Riessen A, Corder GD (2011) Costs and carbon emissions for geopolymer pastes in comparison to ordinary portland cement. *J Clean Prod* 19(9):1080–1090. <https://doi.org/10.1016/j.jclepro.2011.02.010>
- Pacheco-Torgal F, Castro-Gomes B, Jalali S (2008) Alkali-activated binders: a review: Part I. Historical background, terminology, reaction mechanisms and hydration products. *Constr Build Mater* 22(7):1305–1314. <https://doi.org/10.1016/j.conbuildmat.2007.10.015>
- Parrott LJ (1990) Damage caused by carbonation of reinforced concrete. *Mater Struct* 23(3):230–234. <https://doi.org/10.1007/BF02473023>
- Bernal SA, de Gutierrez RM, Provis JL, Rose V (2010) Effect of silicate modulus and metakaolin incorporation on the carbonation of alkali silicate-activated slags. *Cem Concr Res* 40(6):898–907. <https://doi.org/10.1016/j.cemconres.2010.02.003>
- Bernal SA, Provis JL, Walkley B, San Nicolas R, Gehman JD, Brice DG, Kilcullen AR, Duxson P, van Deventer JS (2013) Gel nanostructure in alkali-activated binders based on slag and fly ash, and effects of accelerated carbonation. *Cem Concr Res* 53:127–144. <https://doi.org/10.1016/j.cemconres.2013.06.007>
- Bernal SA, San Nicolas R, Myers RJ, de Gutiérrez RM, Puertas F, van Deventer JS, Provis JL (2014) MgO content of slag controls phase evolution and structural changes induced by accelerated carbonation in alkali-activated binders. *Cem Concr Res* 57:33–43. <https://doi.org/10.1016/j.cemconres.2013.12.003>
- Bernal SA, Provis JL, Brice DG, Kilcullen A, Duxson P, van Deventer JS (2012) Accelerated carbonation testing of alkali-activated binders significantly underestimates service life: the role of pore solution chemistry. *Cem Concr Res* 42(10):1317–1326. <https://doi.org/10.1016/j.cemconres.2012.07.002>
- Bernal SA, Provis JL, De Gutiérrez RM, van Deventer JS (2014) Accelerated carbonation testing of alkali-activated slag/metakaolin blended concretes: effect of exposure conditions. *Mater Struct*. <https://doi.org/10.1617/s11527-014-0289-4>
- Bernal SA, San Nicolas R, Provis JL, De Gutiérrez RM, van Deventer JS (2014) Natural carbonation of aged alkali-activated slag concretes. *Mater Struct* 47(4):693–707. <https://doi.org/10.1617/s11527-013-0089-2>
- Shi C, Roy D, Krivenko P (2006) Alkali-activated cements and concretes. CRC Press, New York
- Xu H, Provis JL, van Deventer JS, Krivenko PV (2008) Characterization of aged slag concretes. *ACI Mater J* 105(2):131–139
- Palacios M, Puertas F (2006) Effect of carbonation on alkali-activated slag paste. *J Am Ceram Soc* 89(10):3211–3221. <https://doi.org/10.1111/j.1551-2916.2006.01214.x>
- Puertas F, Palacios M, Vázquez T (2006) Carbonation process of alkali-activated slag mortars. *J Mater Sci* 41(10):3071–3082. <https://doi.org/10.1007/s10853-005-1821-2>
- Bernal SA, de Gutiérrez RM, Pedraza AL, Provis JL, Rodriguez ED, Delvasto S (2011) Effect of binder content on the performance of alkali-activated slag concretes. *Cem Concr Res* 41(1):1–8. <https://doi.org/10.1016/j.cemconres.2010.08.017>
- Levenspiel O (1999) Chemical reaction engineering. *Ind Eng Chem Res* 38(11):4140–4143
- Jennings HM (2008) Refinements to colloid model of CSH in cement: CM-II. *Cem Concr Res* 38(3):275–289. <https://doi.org/10.1016/j.cemconres.2007.10.006>
- Neto AA, Cincotto MA, Repette W (2008) Drying and autogenous shrinkage of pastes and mortars with activated slag cement. *Cem Concr Res* 38(4):565–574. <https://doi.org/10.1016/j.cemconres.2007.11.002>
- Rahmani O, Highfield J, Junin R, Tyrer M, Pour AB (2016) Experimental investigation and simplistic geochemical modeling of CO₂ mineral carbonation using the mount tawai peridotite. *Molecules* 21(3):353. <https://doi.org/10.3390/molecules21030353>
- Huang H, Ye G (2017) Examining the “time-zero” of autogenous shrinkage in high/ultra-high performance cement pastes. *Cem Concr Res* 97:107–114. <https://doi.org/10.1016/j.cemconres.2017.03.010>
- Kempl J, Çopuroğlu O (2016) EH-pH- and main element analyses of Blast Furnace Slag Cement paste pore solutions activated with sodium monofluorophosphate—Implications for carbonation and self-healing. *Cem Concr Compos* 71:63–76. <https://doi.org/10.1016/j.cemconcomp.2016.05.004>
- Brunauer S, Emmett PH, Teller E (1938) Adsorption of gases in multimolecular layers. *J Am Chem Soc* 60(2):309–319
- Barrett EP, Joyner LG, Halenda PP (1951) The determination of pore volume and area distributions in porous substances. I. Computations from nitrogen isotherms. *J Am Chem Soc* 73(1):373–380
- Clayden NJ, Esposito S, Aronne A, Pernice P (1999) Solid state ²⁷Al NMR and FTIR study of lanthanum aluminosilicate glasses. *J Non-Cryst Solids* 258(1):11–19. [https://doi.org/10.1016/S0022-3093\(99\)00555-4](https://doi.org/10.1016/S0022-3093(99)00555-4)

31. Dimas D, Giannopoulou I, Papias D (2009) Polymerization in sodium silicate solutions: a fundamental process in geopolymerization technology. *J Mater Sci* 44(14):3719–3730. <https://doi.org/10.1007/s10853-009-3497-5>
32. Bernal SA, Provis JL, Rose V, De Gutierrez RM (2011) Evolution of binder structure in sodium silicate-activated slag-meta-kaolin blends. *Cem Concr Compos* 33(1):46–54. <https://doi.org/10.1016/j.cemconcomp.2010.09.004>
33. Kralj D, Brečević L, Nielsen AE (1990) Vaterite growth and dissolution in aqueous solution I. Kinetics of crystal growth. *J Cryst Growth* 104(4):793–800. [https://doi.org/10.1016/0022-0248\(90\)90104-S](https://doi.org/10.1016/0022-0248(90)90104-S)
34. Wu B, Ye G (2017) Development of porosity of cement paste blended with supplementary cementitious materials after carbonation. *Constr Build Mater* 145:52–61. <https://doi.org/10.1016/j.conbuildmat.2017.03.176>
35. Taylor HF (1997) *Cement chemistry*. Thomas Telford, London
36. Ghoulah Z, Guthrie RI, Shao Y (2015) High-strength KOBM steel slag binder activated by carbonation. *Constr Build Mater* 99:175–183
37. Haha MB, Lothenbach B, Le Saout GL, Winnefeld F (2011) Influence of slag chemistry on the hydration of alkali-activated blast-furnace slag-Part I: effect of MgO. *Cem Concr Res* 41(9):955–963. <https://doi.org/10.1016/j.cemconres.2011.05.002>
38. Brough AR, Atkinson A (2002) Sodium silicate-based, alkali-activated slag mortars: part I. Strength, hydration and microstructure. *Cem Concr Res* 32(6):865–879. [https://doi.org/10.1016/S0008-8846\(02\)00717-2](https://doi.org/10.1016/S0008-8846(02)00717-2)
39. Nedeljković M, Zuo Y, Arbi K, Ye G (2018) Natural carbonation of alkali-activated fly ash and slag pastes. In: *High tech concrete: where technology and engineering meet*. Springer, pp 2213–2223. https://doi.org/10.1007/978-3-319-59471-2_253
40. Moerz ST, Knorr K, Huber P (2012) Capillary condensation, freezing, and melting in silica nanopores: a sorption isotherm and scanning calorimetry study on nitrogen in mesoporous SBA-15. *Phys Rev B* 85(7):075403. <https://doi.org/10.1103/PhysRevB.85.075403>
41. Aligizaki KK (2005) *Pore structure of cement-based materials: testing, interpretation and requirements*. CRC Press, London
42. Costoya Fernández MM (2008) Effect of particle size on the hydration kinetics and microstructural development of tricalcium silicate. PhD thesis No. 4102, École Polytechnique Fédérale de Lausanne, Switzerland
43. Houst YF, Wittmann FH (1994) Influence of porosity and water content on the diffusivity of CO₂ and O₂ through hydrated cement paste. *Cem Concr Res* 24(6):1165–1176. [https://doi.org/10.1016/0008-8846\(94\)90040-X](https://doi.org/10.1016/0008-8846(94)90040-X)
44. Xu L, Sahimi M, Tsotsis TT (2000) Nonequilibrium molecular dynamics simulations of transport and separation of gas mixtures in nanoporous materials. *Phys Rev E* 62(5):6942. <https://doi.org/10.1103/PhysRevE.62.6942>
45. Chindaprasirt P, Jaturapitakkul C, Sinsiri T (2005) Effect of fly ash fineness on compressive strength and pore size of blended cement paste. *Cem Concr Comp* 27(4):425–428. <https://doi.org/10.1016/j.cemconcomp.2004.07.003>